

Dynamic Stress Analysis of Sewage Centrifugal Pump Impeller Based on Two-way Coupling Method

PEI Ji*, YUAN Shouqi, and YUAN Jianping

Research Center of Fluid Machinery Engineering and Technology, Jiangsu University, Zhenjiang 212013, China

Received March 21, 2013; revised October 25, 2013; accepted December 31, 2013

Abstract: Current research on the operational reliability of centrifugal pumps has mainly focused on hydrodynamic instability. However, the interaction between the fluid and structure has not been sufficiently considered; this interaction can cause vibration and dynamic stress, which can affect the reliability. In this study, the dynamic stresses in a single-blade centrifugal pump impeller are analysed under different operating conditions; the two-way coupling method is used to calculate the fluid–structure interaction. Three-dimensional unsteady Reynolds-averaged Navier-Stokes equations are solved with the SST $k-\omega$ turbulence model for the fluid in the whole flow passage, while transient structure dynamic analysis is used with the finite element method for the structure side. The dynamic stresses in the rotor system are computed according to the fourth strength theory. The stress results show that the highest stress is near the loose bearing and that the equivalent stress increases with the flow rate because the dynamic stresses are closely related to the pressure load. The stress distributions on the blade pressure side, suction side, leading edge, and trailing edge are each analysed for different flow rates; the highest stress distribution is found on the pressure side. On the blade pressure side, a relatively large stress is found near the trailing edge and hub side. Based on these results, a stress distribution prediction method is proposed for centrifugal pumps, which considers the interaction between the fluid and structure. The method can be used to check the dynamic stress at different flow rates when optimising the pump design to increase the pump reliability.

Keywords: numerical analysis, fluid-structure interaction, single-blade centrifugal pump, dynamic stress

1 Introduction

Single-blade pumps are often used for sewage transport applications. The composition of sewage water, which can contain large portions of fibres and solids, requires this special impeller geometry, in order to avoid operational disturbances from clogging. Strong hydrodynamic phenomena are caused by this unbalanced blade layout, and there is strong interaction between turbulent flow and the impeller structure. Therefore, determining the dynamic stresses on the pump rotor to ensure pump reliability requires both a solution for the flow field in the pump and analysis of the structural mechanics of the pump rotor.

Physically speaking, fluid-structure interaction (FSI) is a natural effect which can be observed throughout the environment. For instance, a palm tree bending in a storm is a kind of FSI. A more technical example is the swinging of a bridge owing to wind^[1–2]. In recent years, there have been multiple reports on FSI in turbomachinery; many were on turbines and compressors, while a few were on pumps. ZHANG, et al^[3–4], used large eddy simulation flow to

examine the FSI in a turbine blade passage; they analysed the vibration characteristics in the frequency domain. CAMPBELL, et al^[5], calculated the deformation of an airfoil in turbomachinery considering FSI and compared the numerical and experimental results. MUENCH, et al^[6], developed a new method for fluid–structure coupling of an oscillating hydrofoil. ZHOU, et al^[7], analysed the dynamic stresses in Kaplan turbine blades under actual operating conditions.

PEI, et al^[8], investigated the flow-induced vibrations of a single-blade sewage water pump impeller under off-design conditions in detail using numerical and experimental methods. They applied different strategies for partitioned FSI simulation of a single-blade pump impeller; the results obtained by one-way and two-way coupling strategies were compared and analysed^[9]. YUAN, et al^[10], combined the calculations for turbulent flow and a vibrating structure using a two-way coupling method to study the effect of FSI in the impeller on the flow field in a centrifugal pump and the transient dynamic behaviour of the rotor structure. KATO, et al^[11], predicted the noise from a multi-stage centrifugal pump using the one-way coupling method. LANGTHJEM, et al^[12], investigated flow-induced noise in a two-dimensional centrifugal pump considering FSI; they believed that the interaction between the fluid and rotating impeller blades has an important role in generating noise. However, few studies have calculated and analysed dynamic stresses in a centrifugal pump caused by an

* Corresponding author. E-mail: jpei@ujs.edu.cn

This project is supported by National Natural Science Foundation of China(Grant Nos. 51239005, 51009072), and National Science & Technology Pillar Program of China(Grant No. 2011BAF14B04)

© Chinese Mechanical Engineering Society and Springer-Verlag Berlin Heidelberg 2014

unsteady hydraulic load owing to a strong FSI effect.

In this study, FSI was simulated to quantify the dynamic stresses for a single-blade centrifugal pump impeller. The two-way coupling method was utilised to realise strong FSI effects during the calculation. The stresses for the pump rotor were calculated under various operating conditions to analyse the relationship between the dynamic stresses and effect on flow rate.

2 Calculation Strategy

To solve the FSI problems properly for engineering applications, several coupling strategies need to be selected and considered based on the characteristics of the problems and feasibility of the coupling algorithm. For instance, in order to account for the fluid mass, which moves with the structure and reduces the frequency of structural vibrations, an acoustic fluid model can be appropriate. In this case, the fluid momentum (Navier-Stokes) and continuity equations are simplified to obtain the acoustic wave equation under the assumption that the fluid is inviscid, and there is no mean flow of the fluid. Harmonic or transient analysis can be performed on the coupled structural-acoustic system. However, if convection, viscosity, or turbulence effects are essential, a full Navier-Stokes CFD solver is generally required. The analysis can be performed by a monolithic or partitioned approach^[13–14]. The monolithic method requires a straightforward solution for all unknowns of the overall coupled system and solves the resulting system of equations with a complete tangent stiffness matrix. All interaction effects between the dependent equations are addressed in one solver. This approach is ideal when the physical interactions are strongly nonlinear; however, it is currently difficult to implement because of severe drawbacks such as the complex modelling required for both fluid and structure fields and the large amount of computational resources required. In the past decades, the partitioned method has been successfully established and applied to practical problems regarding FSI^[15–16]. In this method, the equations governing the flow and displacement of the structure are solved separately in different solvers without any limitations. This allows the advantages of mature solvers to be exploited for both CFD and CSD, precluding the need for developing a specialised solver for FSI problems. The interaction effects between both physical fields are represented by an exchange of loads at the common interface. Therefore, the partitioned approach was adopted in this study.

In the present case, only the pressure force was included in the fluid load. The structural deformation influenced the flow by changing the flow geometry, and the influence of vibration velocity on the moment was not considered. When considering the “critical speed”, modal analysis is important to the initial dynamic analysis. The first natural frequency of the rotor was 127.78 Hz. Compared to the test rotating speed frequency value of 24 Hz, the former is

much greater than the latter. Therefore, no resonance would occur in this case. In addition, the dominant hydrodynamic force component changed slowly compared to the first rotor natural frequency, and the structure’s response may be determined through static analysis. This assumption was clearly confirmed by comparing the results of static and dynamic analyses for the calculated rotor deflection at each time step, as discussed in Ref. [8]; the structure’s response can be assumed to vary slowly with respect to time. Therefore, the above assumption that only the deflection displacement was considered in the coupled calculations is reasonable.

The investigated model pump was a commercial single-stage volute centrifugal pump with a single-blade impeller; the diameter of the pipes at the suction and pressure sides was 100 mm. The impeller outer diameter was 205 mm, and the blade width at the impeller outlet was 100 mm. The cross-section of the flow channel had a minimum free ball passage of 100 mm. Table 1 lists the design parameters of the pump and material characteristic parameters of the rotor structure.

Table 1. Parameters of pump

Design parameter		Material characteristic parameter	
Head H_{des}/m	8	Density $\rho/(kg \cdot m^{-3})$	7850
Flow rate $Q_{des}/(L \cdot s^{-1})$	33.3	Elastic modulus E/GPa	200
Speed $n_{des}/(r \cdot min^{-1})$	1440	Poisson ratio μ	0.3

The water was considered to be incompressible. A time-dependent Reynolds average Navier-Stokes simulation was performed to calculate the flow field in the whole passage of the pump, including the side chamber. The continuity equation and momentum equations for the fluid within a local frame are as follows:

$$\frac{\partial u_i}{\partial x_i} = 0, \quad (1)$$

$$\frac{\partial(\rho u_i)}{\partial t} + \frac{\partial(\rho u_i u_j)}{\partial x_j} = \frac{\partial}{\partial x_j} \left[\mu \left(\frac{\partial u_i}{\partial x_j} + \frac{\partial u_j}{\partial x_i} \right) \right] - \frac{\partial p}{\partial x_i} + \rho f_i, \quad (2)$$

where p is the pressure, ρ is the density, u_i is the velocity vector component, f_i is the body force vector component, and μ is the dynamic viscosity. To close the basic equations, the turbulence was modelled with a $k-\omega$ model using the SST near-wall formulation. The structured grids for the computational domains were generated by using the grid generation tool ICFM-CFD 12.1. The grids of the single-blade impeller are partially shown in Fig. 1, and the number of grid nodes was 2 182 132 in total for both the rotating and stationary domains. A maximum non-dimensional wall distance of $y^+ < 80$ was obtained for the rotor mesh. The impeller side chambers were also included in the grid to take the leakage flow effect into account. The discretisation in space had second-order accuracy, and the second-order backward Euler scheme was

chosen for time discretisation. The interface between the impeller and casing was set to ‘transient rotor-stator’ to capture the transient rotor-stator interaction in the flow; the relative position between the impeller and casing changes for each time step with this kind of interface. A smooth wall condition was used for the wall function. The chosen time step for the transient simulation was $3.472\ 25 \times 10^{-4}$ s at the nominal rotating speed, which corresponds to a change in angle of $\Delta \varphi = 3^\circ$. Within each time step, the iteration stopped when the maximum residual was less than 10^{-3} , and the convergence criterion for the transient problem was when the result reached stable periodicity.

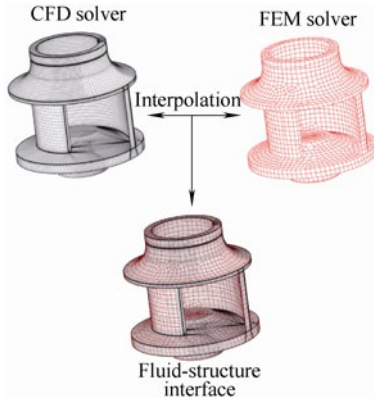


Fig. 1. Data interpolation mapping procedure

The FEM mesh for the structure is shown in Fig. 1; the mesh type was hex-dominant. The transient dynamic equation of interest is

$$\mathbf{M}\ddot{\mathbf{q}}_i(t) + \mathbf{C}\dot{\mathbf{q}}_i(t) + \mathbf{K}\mathbf{q}_i(t) = \mathbf{Q}(t), \quad (3)$$

where $\ddot{\mathbf{q}}_i(t)$ is the nodal acceleration vector, $\dot{\mathbf{q}}_i(t)$ is the nodal velocity vector, $\mathbf{q}_i(t)$ is the nodal displacement vector, \mathbf{M} is the structural mass matrix, \mathbf{C} is the structural damping matrix, \mathbf{K} is the structural stiffness matrix, and $\mathbf{Q}(t)$ is the applied load vector. The Hilber-Hughes-Taylor method was employed for time integration of the transient dynamic equilibrium equation, which is an improved algorithm of the Newmark time integration method. Face-fixed support boundary conditions were used, because the bearing mountings were treated as rigid structures. The dynamic stresses in the rotor system were computed based on the fourth strength theory. Since the shear stress was much smaller than normal stress in this case, the von Mises or equivalent stress σ_{eq} was computed as follows:

$$\sigma_{\text{eq}} = \sqrt{\frac{1}{2}[(\sigma_x - \sigma_y)^2 + (\sigma_y - \sigma_z)^2 + (\sigma_z - \sigma_x)^2]}, \quad (4)$$

The fluid-structure interfaces for all wetted surfaces of the blade, shroud, and hub were defined, including the side chamber wetted surfaces of the shroud and hub; the two sides of the fluid-structure interface for the load transfer had almost the same shape, as shown in Fig. 1. Data interpolation mapping was performed to establish the load transfer system between CFD and FEM solver with fewer

errors because the solid and fluid nodes were not compatible with each other. Through the interfaces, completely different elements and meshes can be used in FSI analysis. The displacement and stress for the fluid node at the FSI boundary was determined by interpolating the displacement and stress of the solid node in the vicinity of the corresponding fluid node. There are two basic conditions for applying fluid-structure interfaces considering the arbitrary Lagrangian Eulerian formulation. The first is the kinematic condition or displacement compatibility, which is as follows:

$$S_f = S_s, \quad (5)$$

$$\mathbf{n} \cdot \boldsymbol{\tau}_f = \mathbf{n} \cdot \boldsymbol{\tau}_s, \quad (6)$$

where S_f and S_s are the fluid and solid displacements, respectively, $\boldsymbol{\tau}_f$ and $\boldsymbol{\tau}_s$ are the fluid and solid stresses, respectively, and \mathbf{n} is the normal vector.

3 Experimental Validation

Experimental data for the model pump were collected at the laboratory of the Institute of Turbomachinery at University of Duisburg-Essen, Germany, to verify the accuracy of the calculation. To measure the radial deflection of the impeller, two B&K SD-051 non-contacting displacement measuring sensors were mounted in two vertical directions on the stationary coordinate frame, and the deflection of the outer side of the suction mouth of the impeller was measured for the test; the numerical oscillation results were obtained from the exact same position.

The impeller oscillation results obtained with the partitioned FSI and experimental methods were qualitatively compared for $Q=33$ L/s, 42 L/s, 22 L/s, 11 L/s. Fig. 2 shows the results for $Q=11$ L/s; the results under the other flow conditions were analysed in Ref. [8]. Although small deviations were observed at some impeller rotating positions for each operating point, good agreement was obtained.

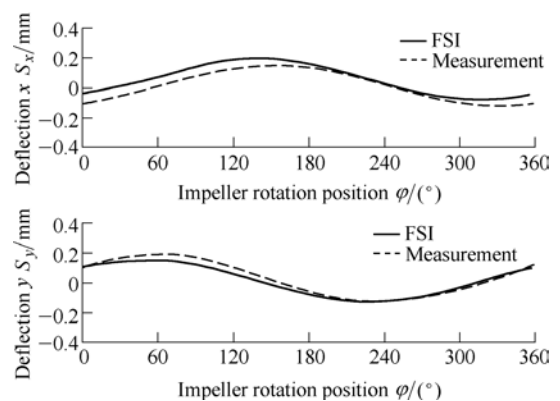


Fig. 2. Calculated and measured impeller oscillation results for $Q=11$ L/s

4 Results and Discussion

In order to analyse the distributions of the dynamic stresses owing to FSI under different conditions, a stationary coordinate frame(x, y) and rotating coordinate frame(ψ, ζ) were defined, as shown in Fig. 3. In addition, to obtain the dynamic stresses as a function of time, P_1 – P_6 were defined as monitoring points on the blade surface at mid-span. P_1 and P_2 were at the pressure and suction sides, respectively, of the blade. P_3 and P_4 were at the leading edge of the blade, while P_5 and P_6 were at the trailing edge of the blade near PS and SS, respectively. The rotation position of the impeller was determined by defining the rotating angle φ between the positive axis ψ of the rotating coordinate frame and positive y axis of the stationary coordinate frame in the clockwise direction; $\varphi=0^\circ$ was obtained when the trailing edge of the impeller was at the top position.

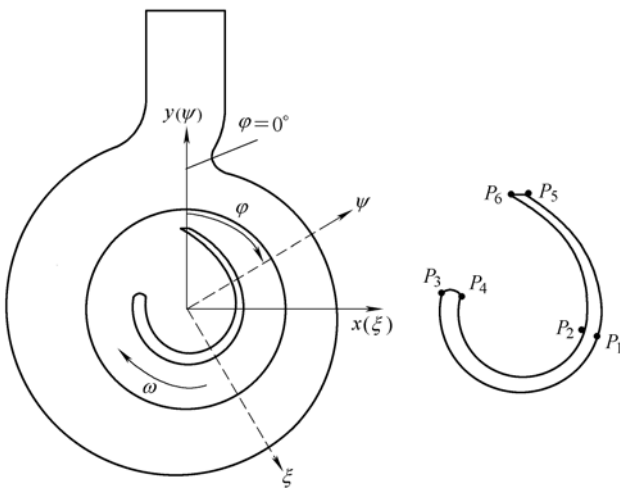


Fig. 3. Definition of coordinate systems and monitoring points

Fig. 4 shows the relative velocity vector distribution at mid-span under the design condition($Q=33$ L/s) when $\varphi=0^\circ$, and the legend represents the velocity scale in the calculation domain. Stable flow patterns were observed in the volute domain, and the velocity was relatively small. Therefore, the kinetic energy of the flow was transformed into pressure energy very well in this volute. Because the circumferential velocity of the domain was zero, the relative velocity was equal to the absolute velocity in the volute. In the rotor domain, an obvious unbalanced velocity distribution was obtained because of the asymmetrical blade shape. A relatively low velocity appeared near the blade pressure side and impeller eye position. A relatively large velocity appeared near the blade suction side and at the circumferential area of the blade outlet; the maximum velocity was at the outermost position of the impeller. The same phenomenon was observed for each examined flow rate.

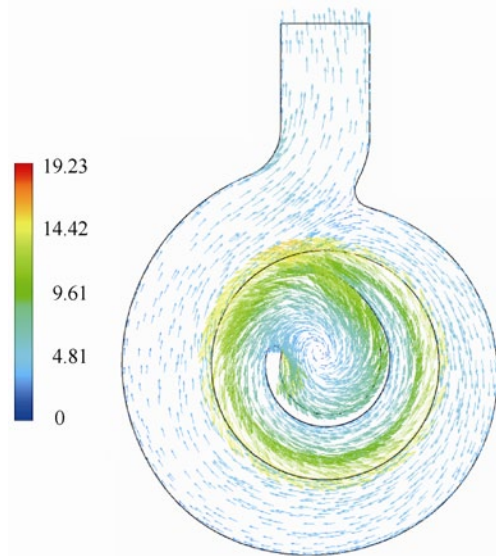


Fig. 4. Relative velocity vector distribution(m/s) at mid-span for $Q=33$ L/s, $\varphi=0^\circ$

The asymmetrical distribution of the flow velocity was followed by an asymmetrical pressure distribution which caused the strong hydrodynamic force acting on the blade, hub, and shroud surfaces, as shown in Fig. 5. Relatively large pressure values appeared not only at the blade pressure side but also at the outer area of the hub and shroud near the blade pressure side. Relatively small pressure values were found at the blade suction side close to the leading edge along the entire blade height. In addition, a pressure gradient was clearly observed on the blade, hub and shroud; the gradient also had an asymmetrical distribution. A relatively large gradient was found at the leading and trailing edges of the blade. During FSI simulation, the pressure distribution was transmitted directly to the FEM model, and the total force obtained by this kind of pressure distribution for each time step was calculated as the boundary condition of the vibration behaviour analysis.

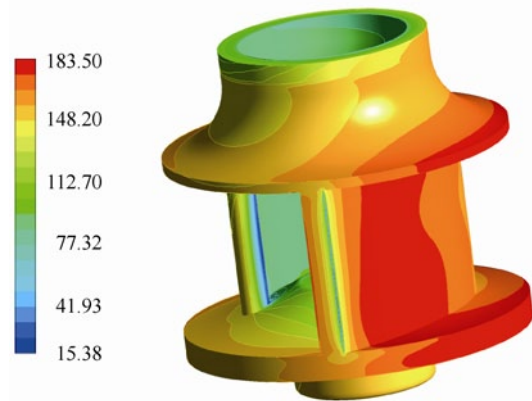


Fig. 5. Pressure distribution (kPa) on impeller surface for $Q=33$ L/s, $\varphi=0^\circ$

Fig. 6 shows the time-dependent maximum equivalent stresses on the rotor structure under different conditions. The maximum value was less than 30 MPa. There was

obvious fluctuation for $Q=33$ L/s, 42 L/s, 11 L/s; little fluctuation was observed for $Q=22$ L/s. The curve for $Q=11$ L/s had a different phase compared with the design and overload conditions, and the biggest value was only slightly larger than the smallest values for the design and large flow rates. For $\varphi=0^\circ-120^\circ$ and $240^\circ-360^\circ$, the value was smaller for the design condition than for the overload condition. Fig. 7 shows the mean values of the maximum equivalent stresses for different flow rates. The biggest value was observed for $Q=42$ L/s; the value increased with the flow rate.

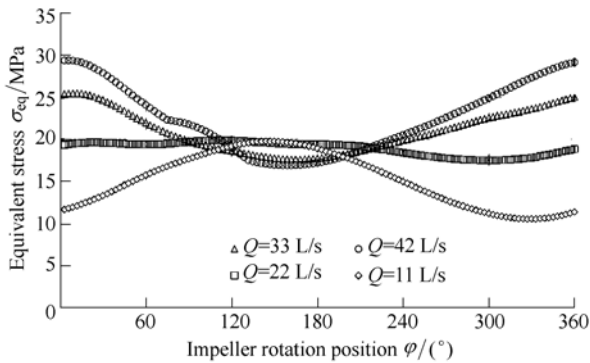


Fig. 6. Time-variant maximum equivalent stresses for different flow rates

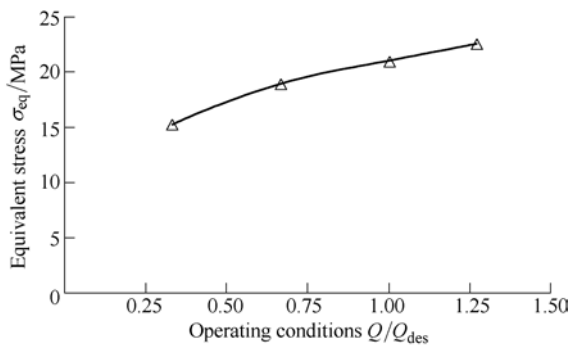


Fig. 7. Mean maximum equivalent stresses for different flow rates

Figs. 8–13 show the equivalent stress distributions at monitoring points P_1 – P_6 on the blade surface at mid-span to evaluate the dynamic stress levels on the blade pressure side, suction side, leading edge, and trailing edge positions for different flow rates. At monitoring point P_1 , which was located on the blade pressure side, relatively large equivalent values of 1–5 MPa were observed. For the other monitoring points, the maximum values were less than 1 MPa. For P_1 , P_2 , and P_4 – P_6 , there was obvious fluctuation at $Q=33$, 42, 11 L/s; a flat distribution curve was observed for $Q=22$ L/s. The curve for $Q=11$ L/s had a different phase compared with that under the design and overload conditions, and almost the same phase could be obtained for the distribution curves at $Q=33$, 42 L/s. For the above monitoring points, relatively small differences in equivalent stress values at each impeller rotating position with the examined flow rates were obtained for $\varphi=120^\circ-240^\circ$, and relatively large differences were observed near $\varphi=0^\circ$. For

P_3 , the flow rate effects on the equivalent stresses appeared to be complex and different from those at the other monitoring points; this may be because the inflow destabilised the flow at the blade leading edge during the impeller revolution, so the flow near the blade leading edge close to the pressure side changed as the function of time with complex roles.

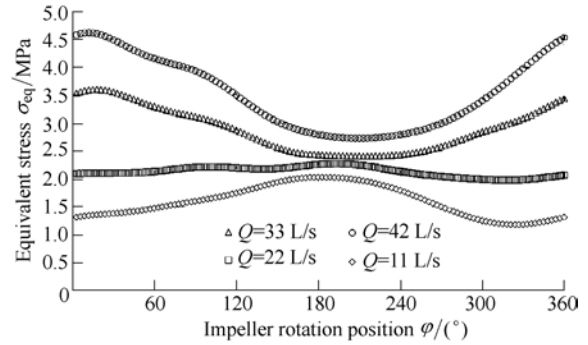


Fig. 8. Time-variant equivalent stresses distribution on P_1 for different flow rates

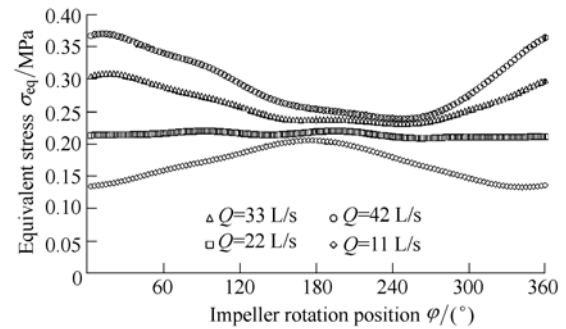


Fig. 9. Time-variant equivalent stresses distribution on P_2 for different flow rates

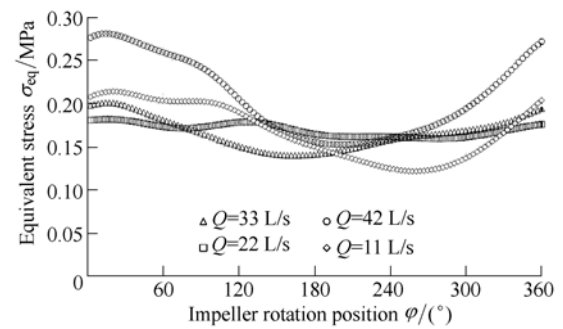


Fig. 10. Time-variant equivalent stresses distribution on P_3 for different flow rates

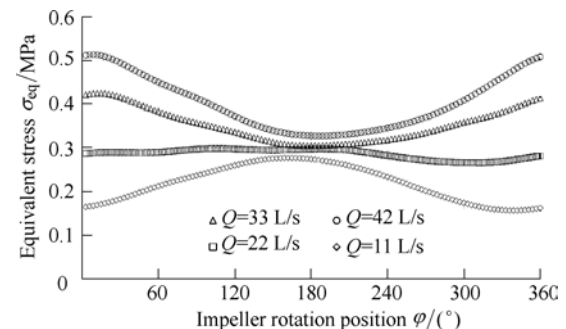


Fig. 11. Time-variant equivalent stresses distribution on P_4 for different flow rates

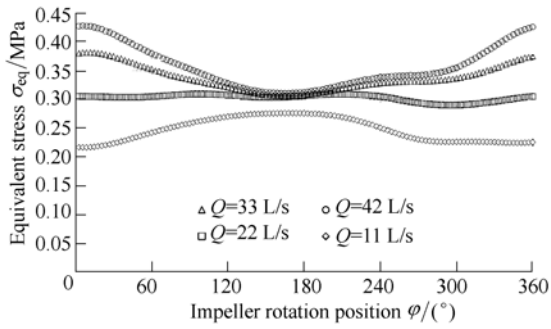


Fig. 12. Time-variant equivalent stresses distribution on P_5 for different flow rates

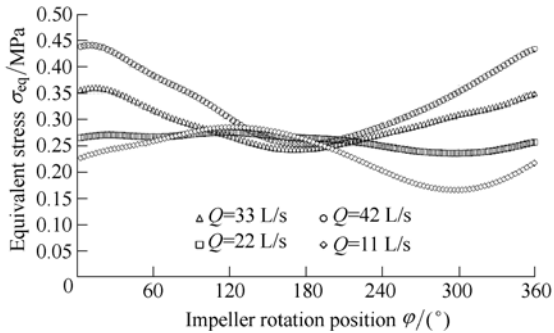


Fig. 13. Time-variant equivalent stresses distribution on P_6 for different flow rates

Fig. 14 shows the equivalent stress distributions around the blade surface at mid-span for different flow rates when $\varphi = 0^\circ$. N represents the serial number of the sampling points, which were numbered sequentially. The positions of the blade trailing edge, blade leading edge, pressure side, and suction side are shown in the figure to demonstrate the equivalent stress distribution behaviours at the specified blade layout position. At the trailing edge (TE), a peak value of equivalent stress was found for each flow rate, and a relatively large gradient was observed. At the position near the leading edge (LE), two peak values were clearly obtained for all conditions. For blade SS, except the section near TE and LE, the equivalent stress decreased gradually from TE to LE, and a clear valley appeared at the section near TE. For the blade PS section, stress values increased from LE to TE except at the section near LE and TE. For most of the positions, the equivalent stress value increased with the flow rate.

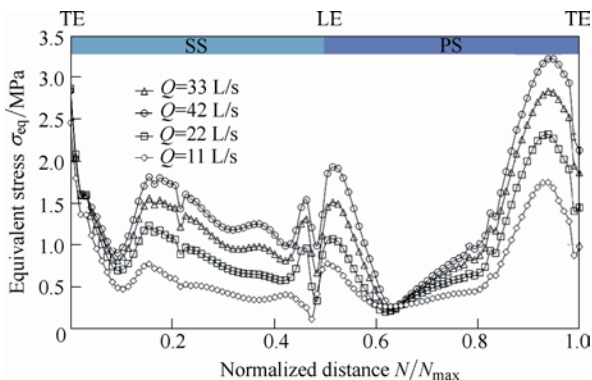


Fig. 14. Equivalent stress distributions around blade at mid-span for different flow rates when $\varphi=0^\circ$

Fig. 15 shows the equivalent stress distributions on the blade cross-section at mid-span at $\varphi = 0^\circ$ under different operational conditions. Relatively large stress values were found in the area near the blade trailing edge, and stress values were relatively small in the area near the blade leading edge. The flow rate clearly affected the equivalent stress distributions; the stress increased with the flow rate.

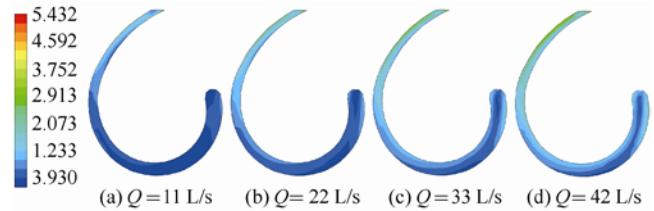


Fig. 15. Equivalent stress distributions (Pa) on blade cross-section at mid-span for different flow rates when $\varphi=0^\circ$

Fig. 16 shows the effect of flow rate on equivalent stress distributions when $\varphi=0^\circ$. Increasing flow rate caused the area of relatively large values to become bigger. For $Q=11$ L/s, there was only a small area of relatively large stress values. For $Q=22$ L/s, this area can clearly be observed at the trailing edge and pressure side near the hub. For $Q=33$ L/s, there was a bigger large value area near the hub, and another area appeared at the trailing edge near the shroud. For $Q=42$ L/s, the biggest area with relatively large values was obtained at the trailing edge and pressure side.

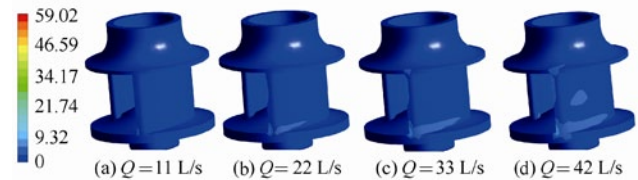


Fig. 16. Flow rate effect on equivalent stress distributions (MPa) when $\varphi=0^\circ$

Fig. 17 shows the equivalent stress distribution on the impeller shaft for $Q=33$ L/s when $\varphi=0^\circ$. The maximum amplitude of the stress distributions of the entire model was on the shaft near where the loose bearing was mounted; the maximum value was more than 40 MPa as obtained by two-way coupling.



Fig. 17. Equivalent stress distribution (MPa) on impeller shaft for $Q=33$ L/s, $\varphi=0^\circ$

5 Conclusions

The dynamic stresses in a single-blade centrifugal pump impeller are calculated for multiple conditions using the FSI strategy with the two-way coupling method. The stress distributions in the rotor are analysed, and the following conclusions are made.

(1) The highest stress is observed near the loose bearing, and the equivalent stress increased with the flow rate because the dynamic stresses are closely related to the pressure load.

(2) The stress distributions on the blade pressure side, suction side, leading edge, and trailing edge are analyzed for different flow rates; the highest stress distribution was found on the pressure side.

(3) On the blade pressure side, a relatively large stress is found near the trailing edge and hub side.

(4) Based on the results, the dynamic stress during the design stage can be predicted while considering the FSI effect. To ensure pump reliability, the dynamic stress results should be checked for large flow rates at least.

Acknowledgements

The authors thank Prof. F.-K. Benra and Dr. H. J. Dohmen from the University of Duisburg-Essen, Germany, for their kind help and providing the model pump.

References

- [1] XING Jingtang, ZHOU Sheng, CUI Erjie. A survey on the fluid-solid interaction mechanics[J]. *Advanced in Mechanics*, 1997, 27(1): 19–38. (in Chinese)
- [2] ZIENKIEWICZ O C, TAYLOR R L. *The finite element method*[M]. Butterworth-Heinemann: Oxford, 2000.
- [3] ZHANG Lixiang, GUO Yakun, WANG Wenquan. FEM simulation of turbulent flow in a turbine blade passage with dynamical fluid-structure interaction[J]. *International Journal for Numerical Methods in Fluid*, 2009, 61(12): 1299–1330.
- [4] ZHANG Lixiang, GUO Yakun, WANG Wenquan. Large eddy simulation of turbulent flow in a true 3D Francis hydro turbine passage with dynamical fluid-structure interaction[J]. *International Journal for Numerical Methods in Fluid*, 2007, 54(5): 517–541.
- [5] CAMPBELL R L, PATERSON E G. Fluid-structure interaction analysis of flexible turbomachinery[J]. *Journal of Fluids and Structures*, 2011, 27(8): 1376–1391.
- [6] MUENCH C, AUSONI P, BRAUN O, et al. Fluid-structure coupling for an oscillating hydrofoil[J]. *Journal of Fluids and Structures*, 2010, 26(6): 1018–1033.
- [7] ZHOU Lingjiu, WANG Zhengwei, XIAO Ruofu, et al. Analysis of dynamic stresses in Kaplan turbine blades[J]. *Engineering Computations*, 2007, 24(8): 753–762.

- [8] PEI J, DOHMEN H J, YUAN S Q, et al. Investigation of unsteady flow-induced impeller oscillations of a single-blade pump under off-design conditions[J]. *Journal of Fluids and Structures*, 2012, 35: 89–104.
- [9] PEI J, BENRA F-K, DOHMEN H J. Application of different strategies of partitioned fluid-structure interaction simulation for a single-blade pump impeller[J]. *Proceedings of the Institution of Mechanical Engineers, Part E: Journal of Process Mechanical Engineering*, 2012, 226(4): 297–308.
- [10] YUAN Shouqi, PEI Ji, YUAN Jianping. Numerical investigation on fluid structure interaction considering rotor deformation for a centrifugal pump[J]. *Chinese Journal of Mechanical Engineering*, 2011, 24(4): 539–545.
- [11] KATO C, YAMADE Y, WANG H, et al. Prediction of the noise from a multi-stage centrifugal pump[C]//*ASME Fluids Engineering Division Summer Meeting*, Houston, Texas, USA, 2005, PART B: 1273–1280.
- [12] LANGTHIEM M A, OLHOFF N. A numerical study of flow-induced noise in a two-dimensional centrifugal pump, part I: hydrodynamics[J]. *Journal of Fluids and Structures*, 2004, 19(3): 349–368.
- [13] FELIPPA C A, PARK K C. Staggered transient analysis procedures for coupled mechanical systems: formulation[J]. *Computer Methods in Applied Mechanics and Engineering*, 1980, 24(1): 61–111.
- [14] PIPERNO S, FARHAT C. Partitioned procedures for the transient solution of coupled aeroelastic problems—part II: energy transfer analysis and three-dimensional applications[J]. *Computer Methods in Applied Mechanics and Engineering*, 2001, 190(24–25): 3147–3170.
- [15] BATHE K J. *Finite element procedures*[M]. Prentice Hall: New Jersey, 1996.
- [16] BATHE K J, ZHANG H, JI S H. Finite element analysis of fluid flows fully coupled with structural interactions[J]. *Computers and Structures*, 1999, 72(1): 1–16.

Biographical notes

PEI Ji, born in 1984, is currently an assistant research fellow at *Research Center of Fluid Machinery Engineering and Technology, Jiangsu University, China*. He received his doctoral degree from *Jiangsu University, China*, in 2013. His research interests include flow instability phenomena and fluid-structure interactions in turbomachines.

Tel: +86-13776474939; E-mail: jpei@ujs.edu.cn

YUAN Shouqi is currently a professor and a PhD candidate supervisor at *Research Center of Fluid Machinery Engineering and Technology, Jiangsu University, China*. He has received 16 prizes for science and technology advancement at the province or ministry level. He has published three books and more than 240 papers. His research interests include the theory, design, and CFD of pumps and fluid machinery.

Tel: +86-511-88780007; E-mail: shouqiy@ujs.edu.cn

YUAN Jianping is currently a professor and a PhD candidate supervisor at *Research Center of Fluid Machinery Engineering and Technology, Jiangsu University, China*. His research interests include drainage and irrigation machinery.

Tel: +86-511-88780280; E-mail: yh@ujs.edu.cn